

Ba(Zn,Co)₂As₂: A diluted ferromagnetic semiconductor with *n*-type carriers and isostructural to 122 iron-based superconductors

Shengli Guo,¹ Huiyuan Man,¹ Kai Wang,¹ Cui Ding,¹ Yao Zhao,¹ Licheng Fu,¹ Yilun Gu,¹ Guoxiang Zhi,¹ Benjamin A. Frandsen,² Sky C. Cheung,² Zurab Guguchia,² Kohtaro Yamakawa,² Bin Chen,³ Hangdong Wang,³ Z. Deng,⁴ C. Q. Jin,⁴ Yasutomo J. Uemura,² and Fanlong Ning^{1,5,*}

¹Zhejiang Province Key Laboratory of Quantum Technology and Device and Department of Physics, Zhejiang University, Hangzhou 310027, China

²Department of Physics, Columbia University, New York, New York 10027, USA

³Department of Physics, Hangzhou Normal University, Hangzhou 310016, China

⁴Beijing National Laboratory for Condensed Matter Physics and Institute of Physics, Chinese Academy of Sciences, Beijing 100190, China

⁵Collaborative Innovation Center of Advanced Microstructures, Nanjing University, Nanjing 210093, China



(Received 26 January 2018; revised manuscript received 25 January 2019; published 2 April 2019)

We report the successful synthesis of a 122 diluted ferromagnetic semiconductor with *n*-type carriers, Ba(Zn,Co)₂As₂. Magnetization measurements show that the ferromagnetic transition occurs up to $T_C \sim 45$ K. Hall effect and Seebeck effect measurements jointly confirm that the dominant carriers are electrons. Through muon spin relaxation, a volume-sensitive magnetic probe, we have also confirmed that the ferromagnetism in Ba(Zn,Co)₂As₂ is intrinsic and the internal field is static.

DOI: [10.1103/PhysRevB.99.155201](https://doi.org/10.1103/PhysRevB.99.155201)

I. INTRODUCTION

The combination of spin and charge degrees of freedom in diluted magnetic semiconductors (DMSs) makes them promising materials for spintronics. The observation of ferromagnetism in Mn-doped III-V GaAs has therefore attracted extensive attention in the last two decades [1–4]. (Ga,Mn)As films are typically fabricated via low-temperature molecular beam epitaxy, where substitution of Mn²⁺ for Ga³⁺ introduces both spins and holes simultaneously. Despite the controversy about the origin of ferromagnetism in (Ga,Mn)As [5], it has been widely accepted that the itinerant carriers mediate the ferromagnetic interaction between spatially separated magnetic ions. To date, the Curie temperature T_C in (Ga,Mn)As has a maximum value of ~ 190 – 200 K [6–8], which is still far below room temperature and therefore limits the possibilities for practical applications. Recently, a series of DMS materials that are structural derivatives of iron-based superconductors was synthesized, including I-II-V Li(Zn,Mn)As [9], 1111 (La,Ba)(Zn,Mn)AsO [10], and 122 (Ba,K)(Zn,Mn)₂As₂ [11]. Of these, (Ba,K)(Zn,Mn)₂As₂ has T_C as high as 180 K [11]. (Ba,K)(Zn,Mn)₂As₂ was synthesized through the doping of K and Mn into the parent semiconductor BaZn₂As₂, where the substitution of Mn for Zn introduces magnetic moments and the substitution of K for Ba introduces carriers. Considering that the end member BaMn₂As₂ is an antiferromagnet with a Néel temperature of 625 K [12], it seems possible that T_C may reach room temperature in 122 systems when the synthesis conditions and the selection of elements are optimized [13].

The above-mentioned DMSs are all *p* type; that is, the dominant carriers are holes. *n*-type DMSs with electron carriers are still exceptionally rare. In practical applications, both *p*- and *n*-type DMSs are required to fabricate junctions and devices. Furthermore, *n*-type DMSs may shed light on the general mechanism of ferromagnetic ordering in DMSs. In the past, Co:ZnO films were proposed to be a candidate for *n*-type DMS [14–16]. However, the underlying mechanism is still under debate. For example, careful investigations showed that the ferromagnetism may arise from a hydrogen-facilitated interaction [17], metallic clusters [18,19], uncompensated spins at the surface of Co-rich antiferromagnetic nanocrystals [20], or bound magnetic polarons [21]. Co:TiO₂ films were also reported to possess ferromagnetism above room temperature, with electrons provided by defects or electric fields acting as carriers [22,23]. A depth-resolved low-energy muon spin relaxation (μ SR) investigation showed that Co:TiO₂ is fully magnetic with intrinsic ferromagnetism [24]. Recently, Hai *et al.* reported the observation of electron-mediated ferromagnetism in (In,Fe)As films, where interstitial Be provides electrons [25–27]. Similar fabrication routes have also been tried in (In,Co)As films, but no ferromagnetic ordering has been observed [28]. Very recently, ferromagnetism above room temperature was also reported in *p*-type (Ga,Fe)Sb and (In,Fe)Sb [29,30]. Theoretically, Gu and Maekawa predicted that *n*-type DMSs may be realized in narrow-band-gap semiconductors [31].

In this paper, we demonstrate the successful synthesis of a high-quality *n*-type ferromagnetic semiconductor by doping Co onto the Zn sites of the narrow-band-gap (0.2 eV) semiconductor BaZn₂As₂ [32]. The highest T_C of Ba(Zn_{1-x}Co_x)₂As₂ reaches ~ 45 K for $x = 0.04$. Using μ SR measurements, we have confirmed the

*ningfl@zju.edu.cn

homogeneous and intrinsic nature of the ferromagnetic ordering in $\text{Ba}(\text{Zn},\text{Co})_2\text{As}_2$.

II. EXPERIMENTAL METHODS

A. Material synthesis

Polycrystalline samples of $\text{Ba}(\text{Zn},\text{Co})_2\text{As}_2$ were synthesized via a solid-state reaction of high-purity ($\geq 99.9\%$) Ba, Zn, Co, and As. Mixed ingredients were placed in alumina crucibles and sealed in evacuated silica tubes. All handling of the elements was conducted in a glove box filled with high-purity Ar (the content of H_2O and O_2 is less than 0.1 ppm) except for the sealing of the silica tubes. The mixture was heated to 900°C for 10 h, then held at 1150°C for 24 h, followed by cooling in the furnace. The products were then ground, pressed into pellets, sealed in evacuated silica tubes, and subsequently heated to 1150°C and held for over 24 h, followed by fast cooling to keep the tetragonal phase.

B. Structural characterization

Powder x-ray diffraction was performed at room temperature using a PANalytical x-ray diffractometer (model EMPYREAN) with monochromatic $\text{Cu } K_{\alpha 1}$ radiation. Energy-dispersive x-ray spectroscopy (EDX) was measured using a field emission scanning microscope (model FEI SIRION-100).

C. Experimental characterization

The dc magnetization measurements were conducted using a Quantum Design magnetic property measurement system (MPMS3). The Hall effect and magnetoresistivity were measured using a Quantum Design physical property measurement system (PPMS). The Seebeck coefficient was measured at room temperature using a commercial thermopower measurement apparatus. The zero-field resistivity was measured via the typical four-probe method with a Keithley 6221 dc and ac current source and Keithley 2182A nanovoltmeter. μSR measurements were performed using the LAMPF spectrometer on the M20 beamline at TRIUMF (Canada), and μSR data were analyzed using the MUSRFIT package [33].

III. RESULTS AND DISCUSSION

A. X-ray diffraction

In Fig. 1(a), we show the x-ray diffraction patterns for $\text{Ba}(\text{Zn}_{1-x}\text{Co}_x)_2\text{As}_2$ with different doping levels. In general, BaZn_2As_2 is polymorphic, typically crystallizing in either an orthorhombic structure (space group $Pnma$) or a tetragonal structure (space group $I4/mmm$) [11]. The tetragonal structure results in a semiconductor with a band gap of ~ 0.2 eV [32] that forms the parent compound of the $(\text{Ba},\text{K})(\text{Zn},\text{Mn})_2\text{As}_2$ DMS system. In this structure, layers of $\{\text{ZnAs}_4\}$ tetrahedra stack alternately with Ba layers along the c axis. We note that if the Zn atoms are replaced by Fe, the resulting material BaFe_2As_2 is the parent compound of many iron-based superconductors [34]. The x-ray diffraction peaks in Fig. 1(a) can be well indexed with a tetragonal structure (space group $I4/mmm$) with no sign of the orthorhombic

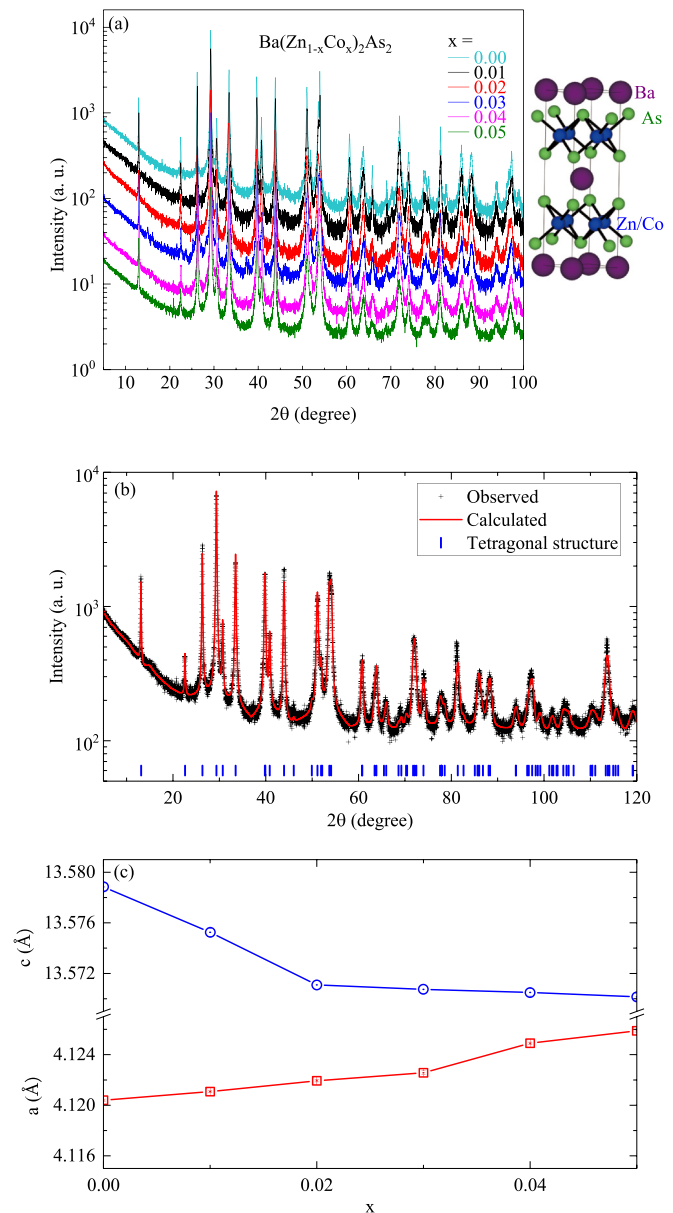


FIG. 1. Structural and x-ray diffraction results. (a) X-ray diffraction patterns of $\text{Ba}(\text{Zn}_{1-x}\text{Co}_x)_2\text{As}_2$ with different doping levels on a semilog scale. The diffraction patterns of $\text{Ba}(\text{Zn}_{1-x}\text{Co}_x)_2\text{As}_2$, with $x = 0.01, 0.02, 0.03, 0.04, 0.05$, are shifted downwards for clarity. (b) Rietveld refinement profile for $x = 0.04$ sample using the GSAS-II package [35]. No obvious impurity peaks were observed, and the resulting weighted reliability factor R_{wp} is $\sim 9.87\%$, indicating a high sample quality. In Fig. 1(c), we show the lattice parameters of different doping levels. With increasing Co concentration a increases, and c decreases monotonically. The monotonic behavior of the lattice parameters indicates the successful doping of Co up to $x = 0.05$. Higher doping does not produce a pure phase, which is also the reason why the resistivity of the $x = 0.05$ sample is larger than that of the $x = 0.04$ sample see Fig. 5(a) below.

phase or other impurities. In Fig. 1(b), we show the Rietveld refinement profile for the $x = 0.04$ sample using the GSAS-II package [35]. No obvious impurity peaks were observed, and the resulting weighted reliability factor R_{wp} is $\sim 9.87\%$, indicating a high sample quality. In Fig. 1(c), we show the lattice parameters of different doping levels. With increasing Co concentration a increases, and c decreases monotonically. The monotonic behavior of the lattice parameters indicates the successful doping of Co up to $x = 0.05$. Higher doping does not produce a pure phase, which is also the reason why the resistivity of the $x = 0.05$ sample is larger than that of the $x = 0.04$ sample see Fig. 5(a) below.

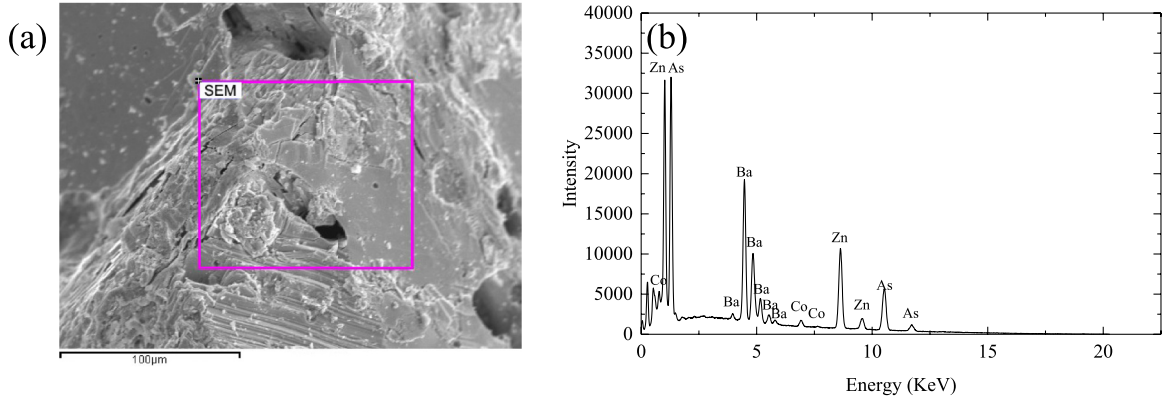


FIG. 2. SEM and EDX of Ba(Zn_{1-x}Co_x)₂As₂ with $x = 0.04$. (a) The surface morphology within the length scale of 100 nm. The rectangle is the test area for EDX. (b) The energy spectroscopy of EDX. The characteristic peaks of Ba, Zn, Co, and As have been marked. Note that the peaks at low energy come from C and O atoms.

B. Energy-dispersive x-ray spectroscopy

In Fig. 2, we show the surface morphology under scanning electron microscopy (SEM) and the energy spectroscopy of EDX for Ba(Zn_{1-x}Co_x)₂As₂ with $x = 0.04$. We select three different areas on the same sample and take the average results as the elemental composition. In Fig. 2(b), we show a typical EDX spectrum. Besides the low-energy peaks which come from the elements C and O adhered on the surface, the other peaks are all indexed by Ba, Zn, Co, and As. We tabulate the atomic percentages in Table I. The ratio of Ba:(Co+Zn):As is close to the chemical formula, and the Co concentration, the ratio of Co:(Co+Zn), is $\sim 4.4\%$, which is consistent with our nominal doping level.

C. Magnetic properties

In Fig. 3(a), we show the temperature-dependent magnetization of Ba(Zn_{1-x}Co_x)₂As₂ ($x = 0.01, 0.02, 0.03, 0.04, 0.05$) in an applied magnetic field of 100 Oe. Zero-field cooling (ZFC) and field cooling (FC) data are represented by open and solid symbols, respectively. For $x = 0.01$, no magnetic transition was observed down to the base temperature of 2 K, and the magnetic moment at 2 K in $H = 100$ Oe is only $0.005\mu_B/\text{Co}$. However, for Co concentrations exceeding 1%, a sudden increase of the magnetization develops around 35–45 K, indicative of a ferromagnetic transition.

We used the Arrott plot method for the precise determination of the Curie temperature T_C for Ba(Zn_{1-x}Co_x)₂As₂ [36]. In Fig. 3(e), we show the Arrott plot for $x = 0.05$. Around T_C ,

TABLE I. The atomic percentages of Ba, Zn, Co, and As in Ba(Zn_{1-x}Co_x)₂As₂ with $x = 0.04$.

	Ba (%)	Zn (%)	Co (%)	As (%)
First	20.93	34.99	1.68	42.40
Second	20.81	37.28	1.67	40.23
Third	24.33	36.53	1.68	40.03
Average	22.02	36.27	1.68	40.03

the points in high magnetic field fall approximately on a series of parallel lines. The solid lines displayed on the plot are the linear fits at high magnetic field, and the nonlinear behavior at low field is ascribed to the higher-order terms we omitted from the analysis or other deviations from mean-field theory. We identify T_C as 41 K, the temperature at which the parallel line would pass through the origin. T_C for other doping levels was also determined by this method (see the Supplemental Material [37]). We list T_C for Ba(Zn_{1-x}Co_x)₂As₂ in Table II. We also obtained the effective moments μ_{eff} by fitting the temperature-dependent magnetization above T_C with a modified Curie-Weiss law: $\chi = \chi_0 + C/(T - \theta)$, where χ_0 is the temperature-independent component, C is the Curie constant, and θ is the Weiss temperature. μ_{eff} is $\sim 1.1\text{--}1.7\mu_B/\text{Co}$. According to $\mu_{\text{eff}} = \mu_B g \sqrt{S(S+1)}$, where μ_B is the Bohr magneton, and assuming the Landé factor $g = 2$, we estimate the average spin state of Co to be close to $S = 1/2$. Due to the contribution of holes and interstitial Mn, the magnetic moment of Mn in (Ga,Mn)As from magnetization measurements was also reported to be less than the expected value of $5\mu_B/\text{Mn}$ [38,39].

In Fig. 3(b), we show the isothermal magnetization at 2 K. Clear hysteresis loops are observed for all doping levels except the paramagnetic $x = 0.01$ sample. The coercive field of Ba(Zn,Co)₂As₂ is on the order of ~ 10 Oe, which is much smaller than the value of 1 T in (Ba,K)(Zn,Mn)₂As₂ [11]. The small coercive field is consistent with the minimal bifurcation of ZFC and FC curves at 100 Oe shown in Fig. 3(a). In Fig. 3(c), we show the temperature dependence of the hysteresis loop for $x = 0.04$. With increasing the temperature, the moment becomes smaller, and the hysteresis loop eventually disappears above 50 K. The saturation moment μ_s is $\sim 0.2\text{--}0.3\mu_B/\text{Co}$ for Ba(Zn,Co)₂As₂, which is much smaller than $2\mu_B/\text{Mn}$ for (Ba,K)(Zn,Mn)₂As₂ and $5\mu_B/\text{Mn}$ for (Ga,Mn)As [2,11].

D. Hall effect, Seebeck effect, and transport

We jointly utilized measurements of the Hall effect and Seebeck effect (see the Supplemental Material) to investigate the properties of the carriers [37]. Since $R_{\text{Hall}} = B/(ne)$, where B is the external field perpendicular to the current and

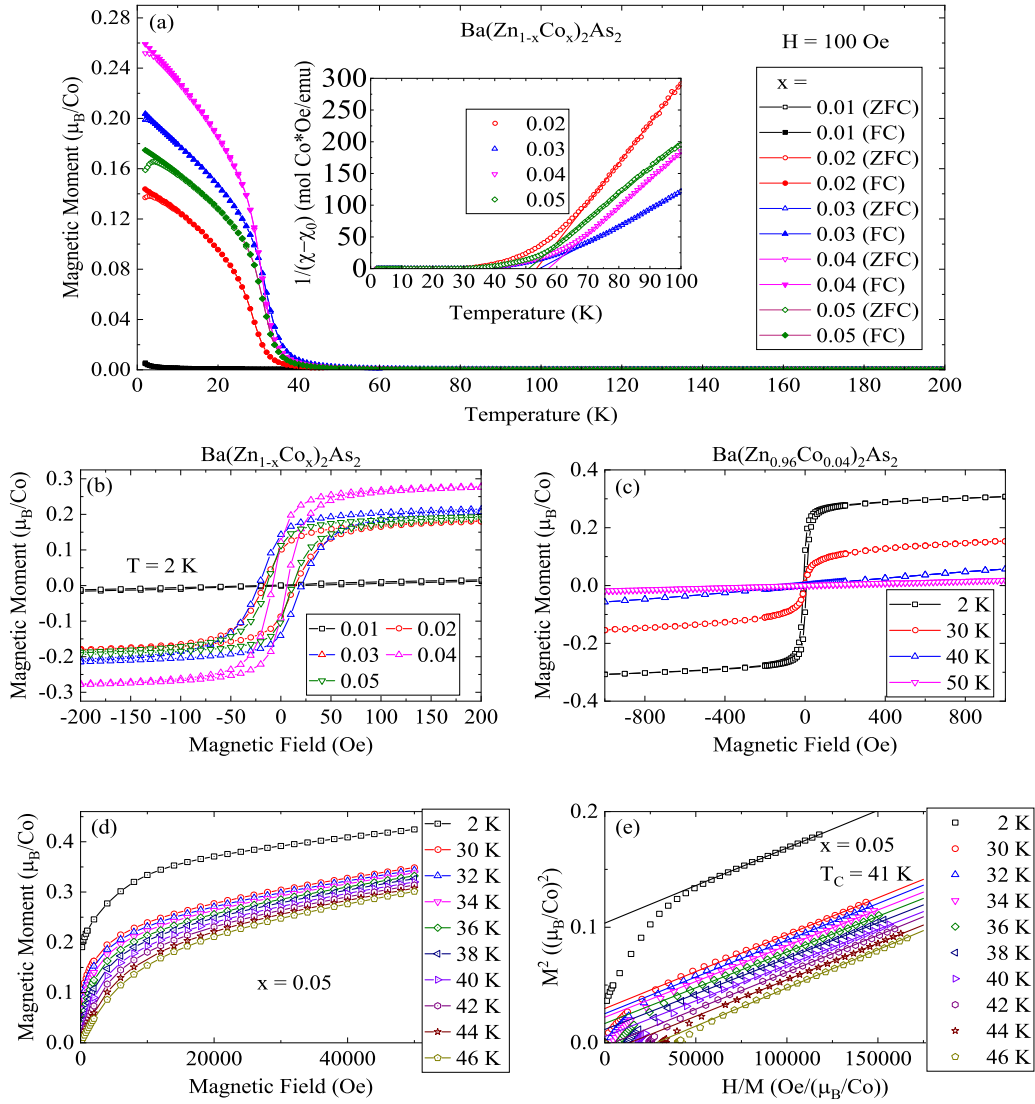


FIG. 3. Magnetization results. (a) The temperature-dependent magnetization of $\text{Ba}(\text{Zn}_{1-x}\text{Co}_x)_2\text{As}_2$ ($x = 0.01, 0.02, 0.03, 0.04, 0.05$) in a magnetic field of 100 Oe. The open and solid symbols represent the zero-field-cooled and field-cooled data, respectively. Inset: Plot of $1/(\chi - \chi_0)$ versus T . Straight lines represent a Curie-Weiss fit. (b) The isothermal magnetization of $\text{Ba}(\text{Zn}_{1-x}\text{Co}_x)_2\text{As}_2$ ($x = 0.01, 0.02, 0.03, 0.04, 0.05$) at 2 K in an applied magnetic field ranging from -200 to 200 Oe. (c) Evolution of the hysteresis loop of $\text{Ba}(\text{Zn}_{0.96}\text{Co}_{0.04})_2\text{As}_2$ with increasing temperature. (d) Isothermal magnetization of $\text{Ba}(\text{Zn}_{0.95}\text{Co}_{0.05})_2\text{As}_2$ at different temperatures. (e) The Arrott plot for $\text{Ba}(\text{Zn}_{0.95}\text{Co}_{0.05})_2\text{As}_2$ at different temperatures. Lines show the best linear fit.

e is the elementary charge, we obtained the carrier concentration from R_{Hall} versus B curves. In Fig. 4, we show the representative Hall resistivity R_H at 25 K and the variation of carrier

density n versus temperature T . Ideally, we should observe the anomalous Hall effect below T_C , but the signal-to-noise ratio is poor in the measurement. Nonetheless, the negative

TABLE II. Curie temperature T_C , Weiss temperature θ and effective moment μ_{eff} (both derived from Curie-Weiss fitting), saturation moment μ_s (the value measured at $T = 2$ K and $H = 200$ Oe), and coercive field H_c .

Co concentration x	T_C (K)	θ (K)	μ_{eff} (in units of μ_B/Co)	μ_s (in units of μ_B/Co)	H_c (Oe)
0.01		0.03	2.0		
0.02	35	53	1.1	0.18	16
0.03	37	54	1.7	0.20	22
0.04	45	57	1.4	0.24	6
0.05	41	51	1.4	0.22	11

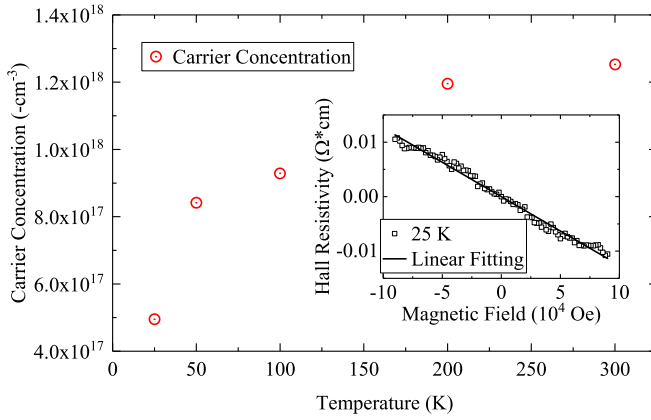


FIG. 4. Results of Hall effect measurements. Carrier concentration of Ba(Zn_{0.96}Co_{0.04})₂As₂ calculated from Hall resistivity curves. The inset displays the Hall resistivity at 25 K, with a linear fit shown by the line.

slope of the Hall resistivity curve indicates that the dominant carriers in Ba(Zn,Co)₂As₂ are electrons. The carrier concentration is roughly estimated to be 10^{17} – 10^{18} /cm³ depending on the measured temperature. This low carrier concentration is comparable to that of Li(Zn,Mn)P and indicates that the electrons introduced by Co doping are mostly localized [40]. The carrier density decreases gradually with decreasing temperature. Seebeck effect measurements at room temperature were also conducted to investigate the carrier type (see the Supplemental Material [37]). The Seebeck coefficient is $S = -\Delta U/\Delta T$, where ΔU is the voltage difference between two electrodes and ΔT is the temperature difference. The sign of the Seebeck coefficient is related to the carrier type, positive for *p*-type carriers and negative for *n*-type carriers. The room-temperature Seebeck coefficient is $\sim -16 \mu\text{V}/\text{K}$ for $x = 0.04$ and $\sim -7 \mu\text{V}/\text{K}$ for $x = 0.05$. The negative Seebeck coefficient confirms our conclusion of *n*-type carriers.

In Fig. 5(a), we show the electrical transport properties for different doping levels. With Co doping, the resistivity retains its semiconducting behavior, but the magnitude decreases, indicating the successful introduction of carriers by Co substitution for Zn. In Fig. 5(b), we show the resistivity in different magnetic fields $R(H)$ for the $x = 0.04$ sample. The $R(H)$ curve decreases clearly below T_C , which is due to the suppression of magnetic scattering by the external field. At $T = 2 \text{ K}$, $R(H)$ reaches a minimum at $H = 6000 \text{ Oe}$, with $[\rho - \rho(0)]/\rho(0)$ reaching $\sim -17\%$, as shown in the inset of Fig. 5(b). This value is much larger than the value of $\sim 7.5\%$ for (Ba,K)(Zn,Mn)₂As₂ at 7 T [41]. Above 6000 Oe, $R(H)$ displays a slight increase with increasing external field. This positive $R(H)$ is from the field-induced spin splitting on disorder-modified electron-electron interactions that has been observed in *n*-type (Zn,Co)O [20]. Nonetheless, the high sensitivity of the resistivity to magnetic field indicates that the electrical transport properties of Ba(Zn,Co)₂As₂ can be easily controlled by external magnetic field.

E. Zero-field and longitudinal field μSR

Generally speaking, a small amount of magnetic impurities such as Co nanoparticles or unknown Co compounds can

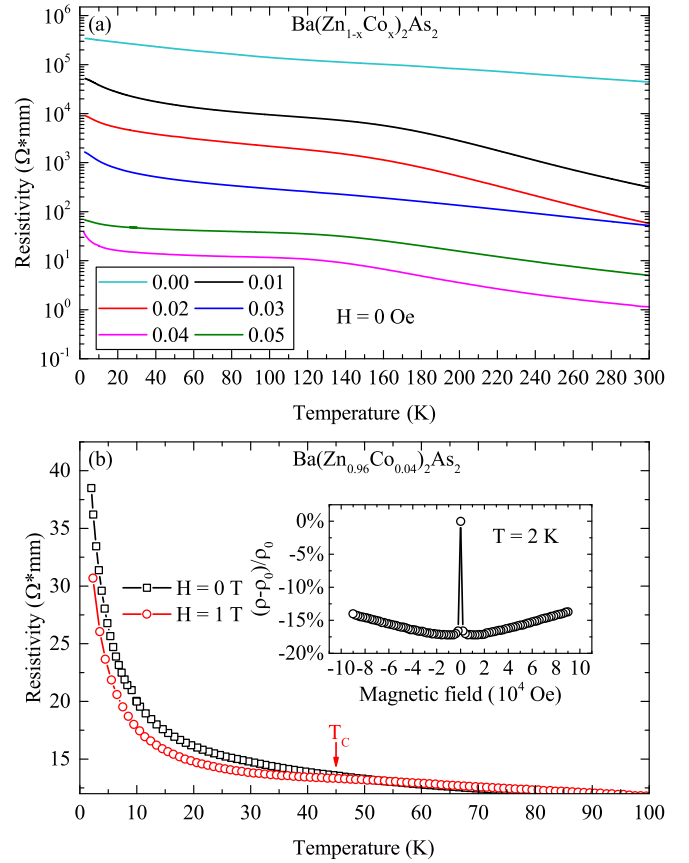


FIG. 5. Results of resistivity measurements. (a) The resistivity as a function of temperature for different doping levels. (b) The temperature dependence of the resistivity for the $x = 0.04$ sample under 0 T and a 1-T magnetic field. The red arrow marks the position of $T_C \sim 45 \text{ K}$. The inset shows $[\rho - \rho(0)]/\rho(0)$ measured at 2 K, with a field interval of 2000 Oe.

give rise to magnetic signals, which may obscure the intrinsic magnetic properties. To rule out such a scenario, we performed μSR , a volume-sensitive magnetic probe, to investigate Ba(Zn,Co)₂As₂. In Fig. 6(a), we show the zero-field (ZF) μSR time spectra for Ba(Zn_{0.95}Co_{0.05})₂As₂. A fast-relaxing component clearly arises below T_C , consistent with the formation of ferromagnetic order. Similar to the case of *p*-type 1111 DMS system (La,Ba)(Zn,Mn)AsO [10], we use a dynamic spin freezing model to fit the ZF- μSR data. As shown by the solid curves in Fig. 6(a), the time spectra can be well fitted by the dynamic-static relaxation function: $A(t) = A_s \left\{ \frac{1}{3} \exp[-(\lambda_d t)^{1/2}] + \frac{2}{3} \left[1 - \frac{a_s^2 t^2}{(\lambda_d t + a_s^2 t^2)^{1/2}} \right] \exp[-(\lambda_d t + a_s^2 t^2)^{1/2}] \right\} g_z(t)$, in which $g_z(t) = \frac{1}{3} + \frac{2}{3} (1 - \Delta^2 t^2) \exp(-\frac{1}{2} \Delta^2 t^2)$ is the static Gaussian Kubo-Toyabe function that describes the nuclear contribution [42]. This indicates that Ba(Zn_{0.95}Co_{0.05})₂As₂ achieves static magnetic order throughout the entire volume at low temperatures, confirming that the previous magnetization measurements are intrinsic to the samples and are not due to a small impurity phase. The static internal field parameter a_s , that is related to the time/frequency window of the probe (μon) and the dynamic relaxation rate λ_d determined from the fits are displayed in Figs. 6(b) and 6(d). The parameter

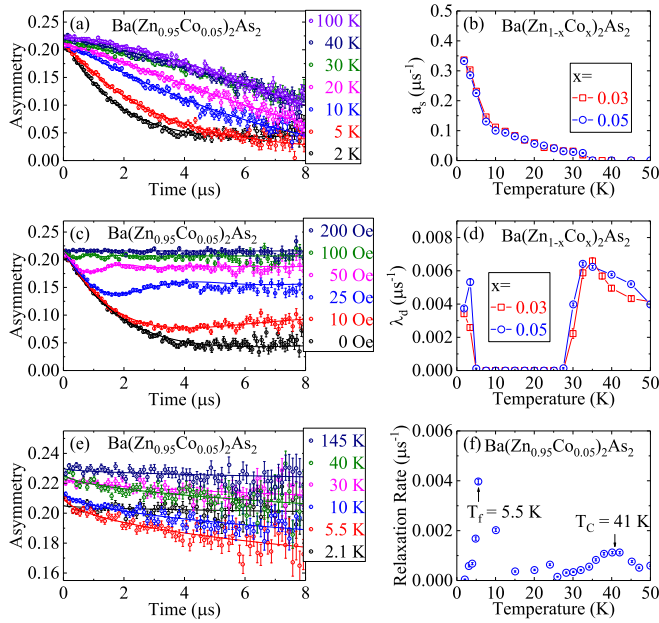


FIG. 6. Results of μ SR characterization. (a) ZF- μ SR time spectra of $\text{Ba}(\text{Zn}_{0.95}\text{Co}_{0.05})_2\text{As}_2$. The solid lines show the best fit to the dynamic-static relaxation function with the static local field amplitude parameter a_s shown in (b) and the dynamic relaxation rate parameter λ_d shown in (d). The LF- μ SR time spectra are shown in (c), exhibiting full decoupling at 200 Oe. (e) The time spectra of LF- μ SR in $\text{Ba}(\text{Zn}_{0.95}\text{Co}_{0.05})_2\text{As}_2$ with an external field of 100 Oe at different temperatures. (f) The muon spin relaxation rate $1/T_1$.

a_s is proportional to the individual ordered moment size multiplied by the moment concentration; a_s is zero above T_C and starts to increase below T_C , indicating the emergence of a static field in the ferromagnetic state.

We used longitudinal field (LF) μ SR to investigate the spin dynamics in $\text{Ba}(\text{Zn},\text{Co})_2\text{As}_2$. In Fig. 6(c), we show the field dependence of the LF- μ SR spectra measured at 2 K. An external field of ~ 100 Oe fully decouples the LF- μ SR time spectra, indicating that the internal magnetic field at the muon stopping sites is fully static and has a magnitude about 10 times lower than the decoupling field, i.e., ~ 10 Oe. In Fig. 6(e), we show the temperature-dependent LF- μ SR spectra conducted under a constant external field of 100 Oe and plot the extracted relaxation rate $1/T_1$ in Fig. 6(f); $1/T_1$ displays behavior similar to that of λ_d obtained from ZF- μ SR [Fig. 6(d)]. The dynamic relaxation exhibits two peaks, one corresponding to T_C arising from the critical slowing down of spin fluctuations near T_C and the other arising at the temperature where ZFC and FC curves start to bifurcate, as shown in Fig. 3(a). This temperature should be related to the freezing of magnetic domains.

F. Discussion

When we plot the static internal field parameter a_s versus T_C in Fig. 7, the point for the present n -type system lies at a location very different from the linear trend shown by many other p -type DMS systems [9–11,43,44]. Since the static internal field parameter a_s is proportional to the concentration multiplied by the average static moment size in dilute spin

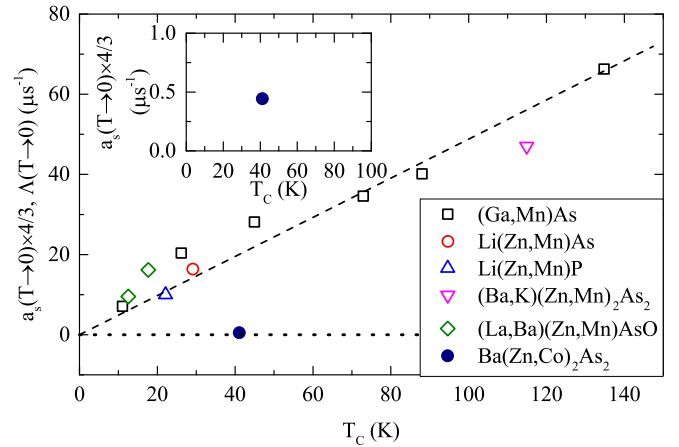


FIG. 7. Plot of a_s versus T_C . Correlation between the static internal field parameter a_s determined at $T = 2$ K by ZF- μ SR and the ferromagnetic Curie temperature T_C observed in (Ga,Mn)As [43], Li(Zn,Mn)As [9], Li(Zn,Mn)P [44], (La,Ba)(Zn,Mn)AsO [10], (Ba,K)(Zn,Mn) $_2$ As $_2$ [11], and $\text{Ba}(\text{Zn},\text{Co})_2\text{As}_2$ (current study). A factor of $4/3$ is multiplied by the parameter a_s to adjust the difference from the simple exponential decay rate Λ adopted in (Ga,Mn)As [43].

systems, the trend for the n -type system implies that T_C is relatively high for the given size and density of the static ordered moments. This tendency can be partly ascribed to the difference between the present Co-doped system and Mn-doped p -type 122 DMS systems, which involve frustration. This is because the nearest-neighbor Mn pairs are coupled antiferromagnetically, as can be seen in BaMn_2As_2 , which is a strong antiferromagnet with $T_N \sim 625$ K [12]. In contrast, BaCo_2As_2 is a paramagnet showing a tendency towards ferromagnetic correlations [45,46]. Therefore, there is no frustration between neighboring Co spins in the Co-doped 122 system. This could lead to the smaller coercive field and stronger ferromagnetic coupling in the n -type system compared to the p -type Mn-doped DMS system. This feature may be helpful for obtaining higher T_C in n -type DMS systems. Another concern we should note is the superparamagnetic-like fragments caused by the fluctuations of the carrier density [47–50]. If the dynamic frequency of these superparamagnetic-like fragments is smaller than the lower-frequency limit of μ SR, which is $\sim 10^4$ Hz, μ SR will treat them as static.

The n -type DMS $\text{Ba}(\text{Zn},\text{Co})_2\text{As}_2$ ($T_C = 45$ K) from the current study joins several related compounds, including the p -type DMS (Ba,K)(Zn,Mn) $_2$ As $_2$ ($T_C = 180$ K; see Table III) [11], the Fe-based superconductor $\text{Ba}(\text{Fe},\text{Co})_2\text{As}_2$ ($T_C = 25$ K) [34], the antiferromagnetic insulator BaMn_2As_2 ($T_N = 625$ K) [12], and the paramagnetic metal BaCo_2As_2 [46]. They all share a common tetragonal crystal structure with a lattice mismatch of less than 5%. Superconducting films of $\text{Ba}(\text{Fe}_{1-x}\text{Co}_x)_2\text{As}_2$ have been fabricated successfully by many groups using pulsed laser deposition methods [51]. Recently, Xiao *et al.* successfully grew high-quality epitaxial films of the tetragonal β - BaZn_2As_2 [32], and Cao is working on the growth of $\text{Ba}(\text{Zn},\text{Co})_2\text{As}_2$ films [52]. With the progress of thin-film growth, it is conceivable that various junctions and devices can be

TABLE III. Comparison of selected properties of (Ga,Mn)As, (Ba,K)(Zn,Mn)₂As₂, and Ba(Zn,Co)₂As₂.

	(Ga,Mn)As	(Ba,K)(Zn,Mn) ₂ As ₂	Ba(Zn,Co) ₂ As ₂
Valence before doping	III-V	II-II-V	II-II-V
Carrier type	holes	holes	electrons
Maximum T_C	190 K [6]	180 K [11]	45 K
Saturation moment	$5\mu_B/\text{Mn}$	$2\mu_B/\text{Mn}$	$0.2\mu_B/\text{Co}$
Sample form	thin film	bulk form	bulk form

fabricated to combine the n -type DMS Ba(Zn,Co)₂As₂, the p -type DMS (Ba,K)(Zn,Mn)₂As₂, and the superconductor Ba(Fe,Co)₂As₂ through the As layers.

IV. CONCLUSION

We have successfully synthesized the ferromagnetic semiconductor Ba(Zn,Co)₂As₂ via the solid-state reaction method. Hall resistivity and Seebeck coefficient measurements jointly confirmed that the carriers in Ba(Zn_{1-x}Co_x)₂As₂ are electrons. Magnetization measurements showed that the highest T_C is ~ 45 K for the 4% doping level and the coercive field is on the order of 10 Oe. ZF- and LF- μ SR measurements showed that a static field arises throughout the full sample volume below T_C , with a magnitude of about 10 Oe at the muon stopping sites. In the temperature-dependent LF- μ SR measurements, we observed a critical slowing down of spin fluctuations around T_C and the freezing of magnetic domains at a lower temperature. Combining the ZF- and LF- μ SR time

spectra, we conclude that the present n -type DMS system exhibits characteristic signatures of dynamic slowing down followed by static magnetic order, with a magnetically ordered state in the entire volume within the time/frequency window.

ACKNOWLEDGMENTS

The work at Zhejiang was supported by MOST (Grant No. 2016YFA0300402), NSF of China (Grant No. 11574265), NSF of Zhejiang Province (Grants No. LR15A040001 and No. LY14A040007), and the Fundamental Research Funds for the Central Universities. Work at Columbia was supported by the NSF (Grants No. DMR 1610633 and No. DMREF DMR-1436095), and the authors acknowledge the JAEA Reimei project. Work at IOPCAS was supported by NSF and MOST through research projects. F.L.N. acknowledges helpful discussions with B. Gu, S. Maekawa, K. Wang, H. Lee, I. Mazin, I. Zutic, and J. Zhao and the help from G. D. Morris, B. S. Hitti, and other staff in the process of μ SR measurements at TRIUMF.

- [1] H. Ohno, A. Shen, F. Matsukura, A. Oiwa, A. Endo, S. Katsumoto, and Y. Iye, *Appl. Phys. Lett.* **69**, 363 (1996).
- [2] H. Ohno, *Science* **281**, 951 (1998).
- [3] I. Zutic, J. Fabian, and S. Das Sarma, *Rev. Mod. Phys.* **76**, 323 (2004).
- [4] T. Jungwirth, J. Sinova, J. Mašek, J. Kučera, and A. H. MacDonald, *Rev. Mod. Phys.* **78**, 809 (2006).
- [5] T. Dietl and H. Ohno, *Rev. Mod. Phys.* **86**, 187 (2014).
- [6] M. Wang, R. P. Campion, A. W. Rushforth, K. W. Edmonds, C. T. Foxon, and B. L. Gallagher, *Appl. Phys. Lett.* **93**, 132103 (2008).
- [7] L. Chen, S. Yan, P. F. Xu, J. Lu, W. Z. Wang, J. J. Deng, X. Qian, Y. Ji, and J. H. Zhao, *Appl. Phys. Lett.* **95**, 182505 (2009).
- [8] L. Chen, X. Yang, F. Yang, J. Zhao, J. Misuraca, P. Xiong, and S. von Molnar, *Nano. Lett.* **11**, 2584 (2011).
- [9] Z. Deng, C. Q. Jin, Q. Q. Liu, X. C. Wang, J. L. Zhu, S. M. Feng, L. C. Chen, R. C. Yu, C. Arguello, T. Goko, F. Ning, J. Zhang, Y. Wang, A. A. Aczel, T. Munsie, T. J. Williams, G. M. Luke, T. Kakeshita, S. Uchida, W. Higemoto, T. U. Ito, B. Gu, S. Maekawa, G. D. Morris, and Y. J. Uemura, *Nat. Commun.* **2**, 422 (2011).
- [10] C. Ding, H. Man, C. Qin, J. Lu, Y. Sun, Q. Wang, B. Yu, C. Feng, T. Goko, C. J. Arguello, L. Liu, B. A. Frandsen, Y. J. Uemura, H. Wang, H. Luetkens, E. Morenzoni, W. Han, C. Q. Jin, T. Munsie, T. J. Williams, R. M. D'Ortenzio, T. Medina, G. M. Luke, T. Imai, and F. L. Ning, *Phys. Rev. B* **88**, 041102(R) (2013).
- [11] K. Zhao, Z. Deng, X. C. Wang, W. Han, J. L. Zhu, X. Li, Q. Q. Liu, R. C. Yu, T. Goko, B. Frandsen, L. Liu, F. Ning, Y. J. Uemura, H. Dabkowska, G. M. Luke, H. Luetkens, E. Morenzoni, S. R. Dunsiger, A. Senyshyn, P. Boni, and C. Q. Jin, *Nat. Commun.* **4**, 1442 (2013).
- [12] Y. Singh, M. A. Green, Q. Huang, A. Kreyssig, R. J. McQueeney, D. C. Johnston, and A. I. Goldman, *Phys. Rev. B* **80**, 100403(R) (2009).
- [13] A. Hirohata, H. Sukegawa, H. Yanagihara, I. Zutic, T. Seki, S. Mizukami, and R. Swaminathan, *IEEE Trans. Magn.* **51**, 1 (2015).
- [14] K. Sato and H. Katayama-Yoshida, *Physica E (Amsterdam, Neth.)* **10**, 251 (2001).
- [15] M. Venkatesan, C. B. Fitzgerald, J. G. Lunney, and J. M. D. Coey, *Phys. Rev. Lett.* **93**, 177206 (2004).
- [16] D. A. Schwartz and D. R. Gamelin, *Adv. Mater.* **16**, 2115 (2004).
- [17] L. Li, Y. Guo, X. Y. Cui, R. Zheng, K. Ohtani, C. Kong, A. V. Ceguerra, M. P. Moody, J. D. Ye, H. H. Tan, C. Jagadish, H. Liu, C. Stampfl, H. Ohno, S. P. Ringer, and F. Matsukura, *Phys. Rev. B* **85**, 174430 (2012).
- [18] R. Boubekri, Z. Beji, K. Elkabous, F. Herbst, G. Viau, S. Ammar, F. Fievet, H. J. von Bardeleben, and A. Mauger, *Chem. Mater.* **21**, 843 (2009).

- [19] M. Sawicki, E. Guzewicz, M. I. Łukasiewicz, O. Proselkov, I. A. Kowalik, W. Lisowski, P. Dłuzewski, A. Wittlin, M. Jaworski, A. Wolska, W. Paszkowicz, R. Jakiela, B. S. Witkowski, L. Wachnicki, M. T. Klepka, F. J. Luque, D. Arvanitis, J. W. Sobczak, M. Krawczyk, A. Jablonski, W. Stefanowicz, D. Sztenkiel, M. Godlewski, and T. Dietl, *Phys. Rev. B* **88**, 085204 (2013).
- [20] T. Dietl, T. Andrearczyk, A. Lipińska, M. Kiecana, M. Tay, and Y. Wu, *Phys. Rev. B* **76**, 155312 (2007).
- [21] L. T. Tseng, A. Suter, Y. R. Wang, F. X. Xiang, P. Bian, X. Ding, A. Tseng, H. L. Hu, H. M. Fan, R. K. Zheng, X. L. Wang, Z. Salman, T. Prokscha, K. Suzuki, R. Liu, S. Li, E. Morenzoni, and J. B. Yi, *Phys. Rev. B* **96**, 104423 (2017).
- [22] Y. Matsumoto, M. Murakami, T. Shono, T. Hasegawa, T. Fukumura, M. Kawasaki, P. Ahmet, T. Chikyow, S. Koshihara, and H. Koinuma, *Science* **291**, 854 (2001).
- [23] Y. Yamada, K. Ueno, T. Fukumura, H. T. Yuan, H. Shimotani, Y. Iwasa, L. Gu, S. Tsukimoto, Y. Ikuhara, and M. Kawasaki, *Science* **332**, 1065 (2011).
- [24] H. Saadaoui, X. Luo, Z. Salman, X. Y. Cui, N. N. Bao, P. Bao, R. K. Zheng, L. T. Tseng, Y. H. Du, T. Prokscha, A. Suter, T. Liu, Y. R. Wang, S. Li, J. Ding, S. P. Ringer, E. Morenzoni, and J. B. Yi, *Phys. Rev. Lett.* **117**, 227202 (2016).
- [25] P. N. Hai, L. D. Anh, S. Mohan, T. Tamegai, M. Kodzuka, T. Ohkubo, K. Hono, and M. Tanaka, *Appl. Phys. Lett.* **101**, 182403 (2012).
- [26] P. N. Hai, L. D. Anh, and M. Tanaka, *Appl. Phys. Lett.* **101**, 252410 (2012).
- [27] P. N. Hai, D. Sasaki, L. D. Anh, and M. Tanaka, *Appl. Phys. Lett.* **100**, 262409 (2012).
- [28] N. T. Tu, L. D. Anh, P. N. Hai, and M. Tanaka, *Jpn. J. Appl. Phys.* **53**, 04EM05 (2014).
- [29] N. T. Tu, P. N. Hai, L. D. Anh, and M. Tanaka, *Appl. Phys. Lett.* **108**, 192401 (2016).
- [30] N. T. Tu, P. N. Hai, L. D. Anh, and M. Tanaka, *arXiv:1706.00735*.
- [31] B. Gu and S. Maekawa, *Phys. Rev. B* **94**, 155202 (2016).
- [32] Z. Xiao, F.-Y. Ran, H. Hiramatsu, S. Matsuishi, H. Hosono, and T. Kamiya, *Thin Solid Films* **559**, 100 (2014).
- [33] A. Suter and B. M. Wojek, *Phys. Procedia* **30**, 69 (2012).
- [34] A. S. Sefat, R. Jin, M. A. McGuire, B. C. Sales, D. J. Singh, and D. Mandrus, *Phys. Rev. Lett.* **101**, 117004 (2008).
- [35] B. H. Toby and R. B. Von Dreele, *J. Appl. Crystallogr.* **46**, 544 (2013).
- [36] A. Arrott, *Phys. Rev.* **108**, 1394 (1957).
- [37] See Supplemental Material at <http://link.aps.org/supplemental/10.1103/PhysRevB.99.155201> for the Arrott plot and Seebeck effect measurements.
- [38] T. Jungwirth, J. Masek, K. Y. Wang, K. W. Edmonds, M. Sawicki, M. Polini, J. Sinova, A. H. MacDonald, R. P. Campion, L. X. Zhao, N. R. S. Farley, T. K. Johal, G. van der Laan, C. T. Foxon, and B. L. Gallagher, *Phys. Rev. B* **73**, 165205 (2006).
- [39] K. Y. Wang, K. W. Edmonds, R. P. Campion, B. L. Gallagher, N. R. S. Farley, C. T. Foxon, M. Sawicki, P. Boguslawski, and T. Dietl, *J. Appl. Phys.* **95**, 6512 (2004).
- [40] Z. Deng, K. Zhao, B. Gu, W. Han, J. L. Zhu, X. C. Wang, X. Li, Q. Q. Liu, R. C. Yu, T. Goko, B. Frandsen, L. Liu, J. Zhang, Y. Wang, F. L. Ning, S. Maekawa, Y. J. Uemura, and C. Q. Jin, *Phys. Rev. B* **88**, 081203(R) (2013).
- [41] K. Zhao, B. Chen, G. Zhao, Z. Yuan, Q. Liu, Z. Deng, J. Zhu, and C. Jin, *Chin. Sci. Bull.* **59**, 2524 (2014).
- [42] Y. J. Uemura, T. Yamazaki, D. R. Harshman, M. Senba, and E. J. Ansaldo, *Phys. Rev. B* **31**, 546 (1985).
- [43] S. R. Dunsiger, J. P. Carlo, T. Goko, G. Nieuwenhuys, T. Prokscha, A. Suter, E. Morenzoni, D. Chiba, Y. Nishitani, T. Tanikawa, F. Matsukura, H. Ohno, J. Ohe, S. Maekawa, and Y. J. Uemura, *Nat. Mater.* **9**, 299 (2010).
- [44] F. L. Ning, H. Man, X. Gong, G. Zhi, S. Guo, C. Ding, Q. Wang, T. Goko, L. Liu, B. A. Frandsen, Y. J. Uemura, H. Luetkens, E. Morenzoni, C. Q. Jin, T. Munsie, G. M. Luke, H. Wang, and B. Chen, *Phys. Rev. B* **90**, 085123 (2014).
- [45] K. Ahilan, T. Imai, A. S. Sefat, and F. L. Ning, *Phys. Rev. B* **90**, 014520 (2014).
- [46] A. S. Sefat, D. J. Singh, R. Jin, M. A. McGuire, B. C. Sales, and D. Mandrus, *Phys. Rev. B* **79**, 024512 (2009).
- [47] M. Sawicki, D. Chiba, A. Korbecka, Y. Nishitani, J. A. Majewski, F. Matsukura, T. Dietl, and H. Ohno, *Nat. Phys.* **6**, 22 (2010).
- [48] L. Chen, F. Matsukura, and H. Ohno, *Phys. Rev. Lett.* **115**, 057204 (2015).
- [49] L. Gluba, O. Yastrubchak, J. Z. Domagala, R. Jakiela, T. Andrearczyk, J. Żuk, T. Wosinski, J. Sadowski, and M. Sawicki, *Phys. Rev. B* **97**, 115201 (2018).
- [50] M. Sawicki, O. Proselkov, C. Sliwa, P. Aleshkevych, J. Z. Domagala, J. Sadowski, and T. Dietl, *Phys. Rev. B* **97**, 184403 (2018).
- [51] S. Haindl, M. Kidszun, S. Oswald, C. Hess, B. Buchner, S. Kolling, L. Wilde, T. Thersleff, V. V. Yurchenko, M. Jourdan, H. Hiramatsu, and H. Hosono, *Rep. Prog. Phys.* **77**, 046502 (2014).
- [52] L. X. Cao (private communications).